PHOTONICS Research

Raman spectroscopy regulation in van der Waals crystals

Wei Zheng,[1,3] Yanming Zhu,[1] Fadi Li,[2] and Feng Huang[1,*]

[1]State Key Laboratory of Optoelectronic Materials and Technologies, School of Materials, Sun Yat-sen University, Guangzhou 510275, China
[2]Key Laboratory of Materials Physics, Institute of Solid State Physics, Chinese Academy of Sciences, Hefei 230031, China
[3]e-mail: zhengw37@mail.sysu.edu.cn
*Corresponding author: huangfeng@mail.sysu.edu.cn

Received 29 June 2018; revised 28 August 2018; accepted 31 August 2018; posted 5 September 2018 (Doc. ID 336335); published 12 October 2018

Raman spectroscopy is a versatile tool widely used for comprehensive probing of crystal information. However, generally when applied in narrow-band-gap van der Waals crystals, it is liable to form a "bug," especially in transition-metal-dichalcogenides (TMDs). That is, several resonant Raman-scattering (RS) modes will inevitably appear in the Raman spectra with strong intensity, interfering with the desired signal of optical-phonon modes. Here, we propose cross-sectional polarized Raman scattering capable of regulating the intensity of RS modes in accordance with quasi-sinusoidal rules. Typically, for MoS_2 and WS_2, when the polarization vector of excited light is along the *c* axis of the crystal, all RS modes are nearly completely "expunged" from the Raman spectra. The mechanism is that the absorption of most TMDs with a space group of R_{3m} for the light polarized along the *c* axis is infinitesimal, thus forming a small coupling intensity of electronic states excited optically and acoustic-phonon modes at point *M*, which in turn restrain the appearance of RS modes. The regulating strategy proposed can be applied to other van der Waals crystals so as to obtain a high signal-to-noise ratio Raman spectrum.

https://doi.org/10.1364/PRJ.6.000991

1. INTRODUCTION

Van der Waals crystals, such as layered semiconductor transition-metal-dichalcogenides (TMDs), are expected to integrate with silicon or other heterogeneous wafers as logic units to realize logical operations [1–3]. In order to fabricate an integrated logic device, the layered TMDs are inevitably bonded to other functional materials such as metal, organics, dielectrics, and semiconductors [4–6]. However, the bonding process may incite a potential problem: due to their small crystal lattice energy, van der Waals TMDs are liable to trigger crystal lattice distortion in the environment of a heterogeneous interface, thus resulting in some unpredictable optoelectronic properties and reducing the reliability of the TMD-based logic device [5,7]. Therefore, a non-destructive and *in situ* tool is needed to probe into the TMDs in the micro-zone and to provide accurate information about the changes in their lattice structure and optoelectronic properties.

Micro-Raman spectroscopy, meeting the above requirements, is an ideal tool for probing van der Waals crystals [8–10]. It has already been widely used to measure the crystallinity, number, and orientation of layers [11,12] and the types and quality of edges [13], as well as to analyze the perturbation effect under strain, doping, or electromagnetic conditions [8]. In spite of such extensive applications, Raman spectroscopy still has a "bug" for probing narrow-band-gap TMDs. Generally, a large number of resonant Raman-scattering (RS) modes, coming from the coupling of acoustic-phonon modes at point *M* and optically excited electronic states, occur in Raman spectra, which interfere optical-phonon (OP) modes under conventional excitation conditions (λ_{exc} =532,633 nm). This bug significantly decreases the signal-to-noise ratio (SNR) of Raman spectra in typical TMDs such as MoS_2 and WS_2 [9,14–16].

As mentioned before, resonant Raman scattering in semiconductors mainly comes from the coupling of acoustic phonon modes and electronic states excited by photons. Thus, to eliminate the RS mode, it is necessary to inhibit the absorption of excited light in the measured crystals as much as possible. Here, typically for MoS_2 and WS_2, we first figure out the anisotropic absorption characteristics comprehensively within the visible light range via first-principles calculations. The results indicate that both MoS_2 and WS_2 have infinitesimal absorption for out-of-plane polarized light ($\boldsymbol{e}_i \| \boldsymbol{c}$ axis), even if the excited photon energy exceeds the band gap. Based on theoretical understanding, we achieve a quasi-sinusoidal control of the scattering intensity in RS modes under the cross-sectional scattering geometry configuration, realize an almost complete suppression of the

RS modes, and obtain Raman spectra with ultra-high SNR. The strategy used in this research of combining theory and experimental research can be also extended to the regulation and suppression of RS modes in other van der Waals crystals.

2. EXPERIMENTAL RESULTS AND DISCUSSION

The two typical van der Waals crystals for Raman regulation in this work, MoS_2 and WS_2, have an indirect bandgap of 1.5 eV and 1.4 eV, respectively [17,18]. In normal Raman-scattering measurements, usually, the excited laser wavelength is 532 nm and/or 633 nm, and with the wave vector $\boldsymbol{k}_i$ along the $\boldsymbol{c}$ axis of crystals (i.e., $\boldsymbol{k}_i \| \boldsymbol{c}$ axis, $\boldsymbol{e}_i \perp \boldsymbol{c}$ axis), any excited light polarized in-plane produces strong RS modes [8,14,15], as shown in Fig. 1. Obviously, the obtained typical Raman spectra contain a large number of RS modes, causing difficulties in identifying the lattice-distortion-sensitive OP modes [19,20], such as A_{1g}.

As mentioned earlier, the resonant Raman-scattering intensity is strongly dependent on the absorption of excited lights (absorption mainly comes from the electronic transitions). To understand the scattering behavior of RS modes in van der Waals crystals, it is necessary to probe into the anisotropic optical absorption characteristics systematically. Therefore, first we apply the first-principles method to calculate the absorption characteristics of MoS_2 and WS_2 to visible lights with different polarizations via the Perdew–Burke–Ernzerhof functional [21], and the results are shown in Fig. 2.

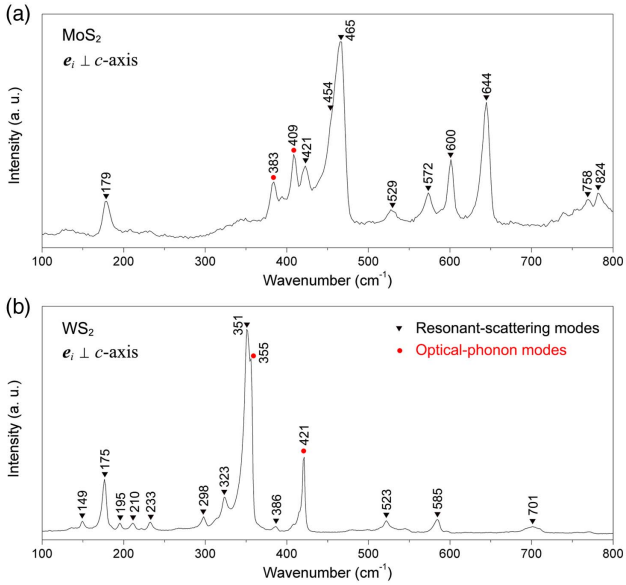

Fig. 1. Typical Raman spectra of MoS_2 and WS_2 scattering from in-plane ($\boldsymbol{e}_i \perp \boldsymbol{c}$ axis). (a) Typical Raman-scattering spectrum of MoS_2 excited by a 633 nm laser, and a large number of LA(M)-related RS modes are excited. All recoded modes in MoS_2 Raman spectroscopy are identified as 179 [$A_{1g}(M) + LA(M)$], 383 [$E^1_{2g}(\Gamma)$], 409 [$A_{1g}(\Gamma)$], 421 [$B^2_{2g} + E^2_{1u}(\Gamma - A)$], 454 [2LA($M$)], 465 [$A_{2u}(\Gamma)$], 529 [$E_{1g}(M) + LA(M)$], 572 [$2E_{1g}(\Gamma)$], 600 [$E^1_{2g}(M) + LA(M)$], 644 [$A_{1g}(M) + LA(M)$], 767 (unknown), 785 (unknown), and 824 (unknown) cm^{-1} [14,16]. (b) Typical Raman-scattering spectrum of WS_2 excited by a 532 nm laser, and the recoded modes are identified as LA(M) at 175 cm^{-1}, $E^1_{2g}(M)$ – LA(M) at 195 cm^{-1}, $A_{1g}(M)$ – LA(M) at 233 cm^{-1}, 2LA(M) – $2E^2_{2g}(M)$ at 298 cm^{-1}, $E_{1g}(M)$ at 323 cm^{-1}, 2LA(M) at 351 cm^{-1}, $A_{1g}(\Gamma)$ at 421 cm^{-1}, $E^1_{2g}(M) + LA(M)$ at 523 cm^{-1}, $A_{1g}(M) + LA(M)$ at 585 cm^{-1}, and 4LA(M) at 701 cm^{-1} [9].

The results in Fig. 2 indicate that MoS_2 and WS_2 show no optical absorption anisotropy in-plane [Figs. 2(c) and 2(d)] yet boast strong anisotropy in the cross section [Figs. 2(a) and 2(b)]. Importantly, when the electric vector is along the $\boldsymbol{c}$ axis ($\boldsymbol{e}_i \| \boldsymbol{c}$ axis, i.e., $\theta = 0$ or π), the absorption coefficient is close to zero, and it is also weakly related to photon energy, even for those whose energy is greater than the band gap.

The calculation results can be further clarified by a physical description as follows [22]. The electrons in the plane of layered MoS_2 and WS_2 can move freely and interaction with the photons' polarization lies in-plane. For example, the conduction-band minimum (CBM) of layered WS_2 is predominately constructed by W dz^2 orbitals, whereas the valence-band maximum (VBM) constructed by W dxy and $dx^2 - y^2$ orbitals, leaves only a small amount of room for S px and py orbitals to contribute [23]. On the one hand, once the incident photon polarization lies in-plane along the $\boldsymbol{a}$ axis (corresponding to the $\boldsymbol{x}$ axis in mathematics), the absorption coefficient can be calculated by $\alpha_a = |\langle \mathrm{CBM}|x|\mathrm{VBM}\rangle|^2 = |\int dxdydzz^2x^2|^2$. The even integrand and the finite integral indicate that an oscillation between the W dz^2 orbital and the S px orbital of electron density is induced by the photon polarized in-plane. Thereafter, it brings about a bright transition, absorbing the incident photons. On the other hand, if incident photon polarization is placed along the $\boldsymbol{c}$ axis (corresponding to the $\boldsymbol{z}$ axis in mathematics), the integrand will be odd, written as $\alpha_c = |\langle \mathrm{CBM}|x|\mathrm{VBM}\rangle|^2 = 0$, and the absorption coefficient will reach zero. From the above explanation, it is clear that optical absorption cannot be brought by photons polarized out-of-plane. MoS_2, too, follows similar procedures.

These theoretical results give guidelines for designing a Raman-scattering geometric configuration to suppress RS modes.

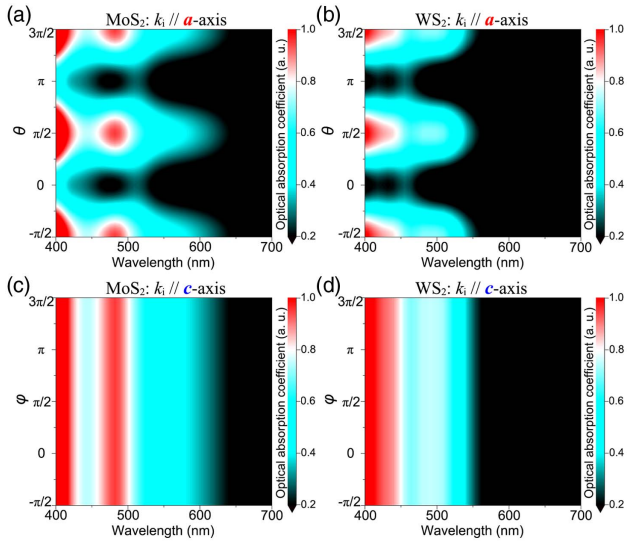

Fig. 2. Normalized optical absorption coefficients of the cross section ($\boldsymbol{k}_i \| \boldsymbol{a}$ axis) in (a) MoS_2 and (b) WS_2 calculated via first principles, where ordinate θ is the angle between the incident light polarized vector $\boldsymbol{e}_i$ and the $\boldsymbol{c}$ axis of the crystals. The absorption coefficients of the in-plane area ($\boldsymbol{k}_i \| \boldsymbol{c}$ axis) in (c) MoS_2 and (d) WS_2, where the ordinate φ represents the angle between the incident light $\boldsymbol{e}_i$ and the $\boldsymbol{c}$ axis.

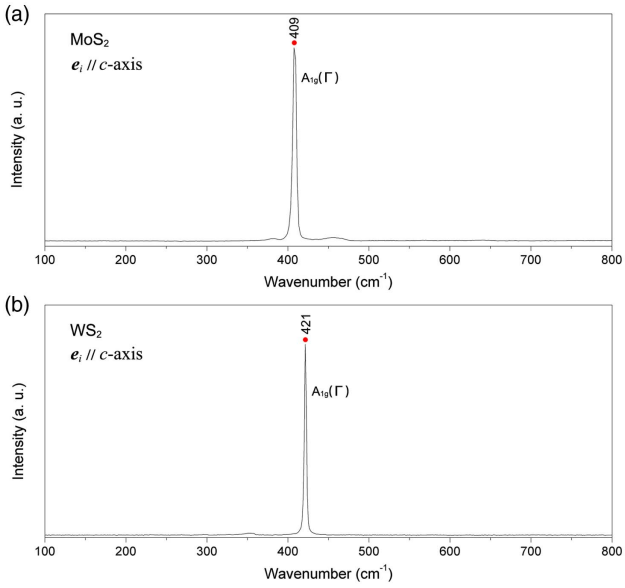

Fig. 3. Improved Raman spectra of (a) MoS_2 and (b) WS_2 scattering from out-of-plane polarization ($\boldsymbol{e}_i \| \boldsymbol{c}$ axis). Compared to Fig. 1, the RS modes here are fully suppressed and the high SNR of the OP mode is highlighted.

Based on the understanding of optical absorption in Fig. 2, we conduct Raman measurements on MoS_2 and WS_2 again under an $\boldsymbol{x}(\boldsymbol{z}-)\boldsymbol{x}$ geometric configuration. The expected Raman spectra with a high SNR is obtained, and RS modes are nearly inhibited, as shown in Fig. 3. It is noteworthy that under such an out-of-plane polarization geometric configuration, unlike the increased intensity of $A_{1g}(\Gamma)$, the scattering intensity of $E^1_{2g}(\Gamma)$ is weakened, regulated by the Raman selection rules.

To provide a clear explanation for the above satisfactory experimental results, it is necessary to conduct a systematic study of the evolution of RS modes when van der Waals MoS_2 and WS_2 are under different polarization conditions. In response, we carry out the following polarized Raman-scattering measurements comprehensively. Figures 4(a) and 4(b) show the cross-sectional angle-dependent polarized (CAP) Raman spectra, boasting strong anisotropy, while Figs. 4(c) and 4(d) show the in-plane angle-dependent polarized (IAP) Raman spectra, bearing almost no anisotropy.

It can be found through careful observation that OP and RS modes in Figs. 4(a) and 4(b) display distinct anisotropic behaviors. The relationship between the scattering intensity of the A_{1g} OP mode and θ is close to the quasi-sine wave [details are shown in Figs. 5(a) and 5(b)], while the RS modes the quasi-cosine wave [Figs. 5(c) and 5(d)].

The anisotropic scattering behavior of the OP mode A_{1g} accords with the Raman selection rule tightly, i.e., $I \sim |\boldsymbol{e}_s \cdot \boldsymbol{R} \cdot \boldsymbol{e}_i|^2$ [22,24–27], where I is Raman-scattering intensity, $\boldsymbol{e}_i$ is the polarization of incident light, $\boldsymbol{e}_s$ is the polarization of scattering light, and $\boldsymbol{R}$ is the Raman tensor. For the current measured crystals and geometric configuration, the Raman tensor is

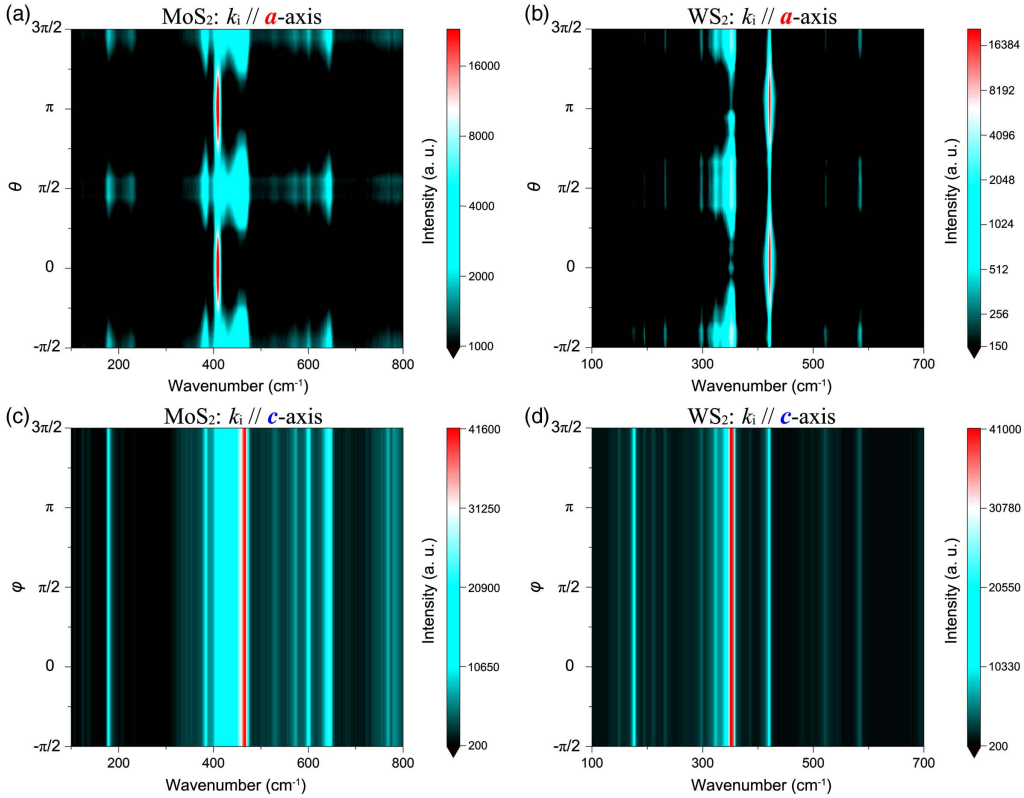

Fig. 4. The cross-sectional angle-dependent polarized (CAP) Raman spectra of (a) MoS_2 and (b) WS_2, where the ordinate θ is defined as the angle between the incident light polarization $\boldsymbol{e}_i$ and the $\boldsymbol{c}$ axis, and the in-plane angle-dependent polarized (IAP) Raman spectra of (c) MoS_2 and (d) WS_2, where the ordinate φ is defined as the angle between the incident light polarization $\boldsymbol{e}_i$ and the $\boldsymbol{a}$ axis.

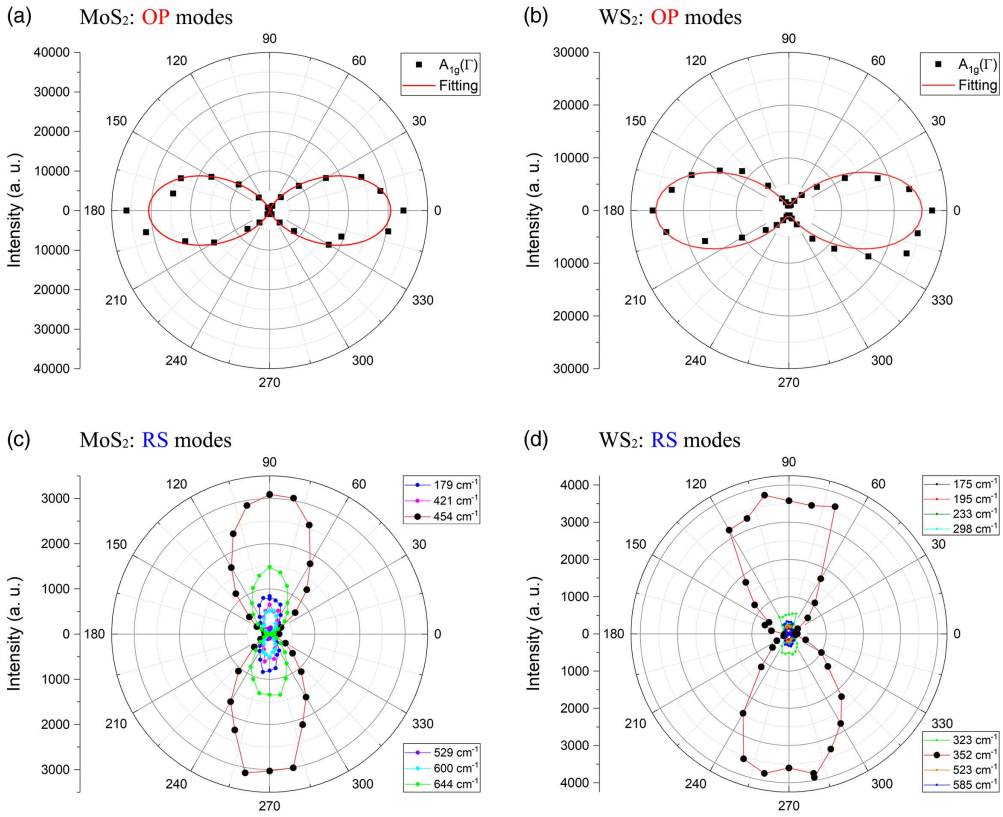

Fig. 5. Raman intensities of OP and RS modes extracted from Figs. 4(a) and 4(b) via Lorentzian fitting. (a) and (b) display angle-dependent intensities of A_{1g} OP modes in MoS_2 and WS_2, respectively, and reveal a similar changing rule in MoS_2 and WS_2. The red line gives the corresponding fitting results based on the Raman selection rule, i.e., Eq. (1). (c) and (d) show the angle-dependent intensities of resonant scattering modes in layered MoS_2 and WS_2, respectively. All modes appear with the same θ angle dependence: when $\theta = (n + 1/2)\pi$, the scattering intensity reaches the highest value; while $\theta = n\pi$, the value approximates to zero.

$$\boldsymbol{R}[\mathrm{A}_{1g}] = \begin{bmatrix} a & & \\ & a & \\ & & be^{i\Phi} \end{bmatrix}, \tag{1}$$

$$\boldsymbol{e_i} = \boldsymbol{e_s} = \begin{pmatrix} \sin\theta \\ 0 \\ \cos\theta \end{pmatrix}. \tag{2}$$

Thus, the Raman-scattering intensity of the A_{1g} mode is derived as follows:

$$I_{\mathrm{A}_{1g}}(\theta) \sim |a|^2 \sin^4\theta + |c|^2 \cos^4\theta + \frac{1}{2}|a||c|\sin^2(2\theta)\cos\Phi,$$

where Φ is defined as the apparent phase [28]. The matched fitting results in Figs. 5(a) and 5(b) show that the formula can elaborate the anisotropic behaviors of A_{1g} modes well.

However, Raman selection rules cannot describe the anisotropic behaviors of RS modes because they do not originate from the Raman-activated optical phonon. The RS modes are derived from the coupling intensity of optical excited electronic states and acoustic phonon modes at point M, so the light absorption coefficient can reasonably be used to explain the anisotropic behaviors of RS modes.

The scattering intensities of the RS modes in Figs. 5(c) and 5(d) completely reproduce anisotropic distribution of the optical absorption coefficients in Figs. 1(a) and 1(b). When the excited light polarization is perpendicular to the $\boldsymbol{c}$ axis of the crystals (i.e., $\theta = \pi/2$ or $3\pi/2$), the corresponding light absorption reaches the maximum value, which in turn makes the intensities of all the RS modes attain the maximum value. When the polarization is parallel to the $\boldsymbol{c}$ axis of the crystals (i.e., $\theta = 0$ or π), the light absorption attains the minimum value, resulting in the minimum RS mode intensities. Thus, the RS modes could be almost submerged in the background of Raman spectra, ensuring that the obtained Raman spectra have an ultra-high SNR. This strategy of Raman spectroscopy regulation can also be extended to other van der Waals crystals as an ideal tool for exploring and analyzing crystals' quality and orientation, number of layers, types of edges, and effects of perturbations.

3. CONCLUSION

We propose a Raman regulation method or strategy to inhibit the occurrence of RS modes in the Raman spectra of van der Waals crystals and to obtain the desired Raman spectra with a high SNR. More specifically, when the polarization of excited light is along the $\boldsymbol{c}$ axis of crystals, the long-awaited improved Raman spectra containing only OP modes without any RS modes are achieved. The mechanism is that, under out-of-plane polarization, most TMDs with a space group of R_{3m} will produce an extremely weak light absorption and, anomalously, an extremely strong Raman scattering of A_{1g} OP modes.

4. METHODS

A. First-Principles Calculation

All density functional calculations are performed via the Vienna Ab-initio Simulation Package (VASP), using the Perdew–Burke–Ernzerhof functional [21]. The plane-wave energy cutoff for all the calculations is 680 eV. The lattice constants with a Monkhorst–Pack k-grid of $7 \times 7 \times 1$ are not fully relaxed until the energy difference between two successive iterations is lower than 10^{-5} eV and the forces on every atom are lower than 10^{-3} eV/Å (1Å = 0.1 nm) [29]. GW calculations of optimized bulk structures are used to obtain electronic absorption spectra of linearly polarized light. The polarization absorption coefficient formula is written as $\alpha(\theta) = \alpha_c + (\alpha_c - \alpha_a)\sin^2\theta$ [30], where α_c is the absorption coefficient of the polarization vector parallel to the layers, while α_a is that of the polarization vector perpendicular to the layers.

B. Raman-Scattering Measurements

MoS_2 and WS_2 samples are the ideal crystals for commercial use. CAP Raman measurements on MoS_2 and WS_2 are carried out via a Renishaw micro-Raman spectrometer (inVia Reflex) in backscattering geometry, using 633 nm and 532 nm lasers with a power of 0.25 mW and 0.3 mW, respectively. For CAP Raman-scattering measurement, the incident excitation laser focuses on the cross section of MoS_2 (WS_2), which is laid on a rotating stage by a 50× objective lens; the rotating angle θ is noted as the angle between the polarization vector $\boldsymbol{e_i}$ of incident light and the $\boldsymbol{c}$ axis of the crystals. For IAP Raman-scattering measurement, the incident excitation laser focuses on the in-plane area of MoS_2 (WS_2); the rotating angle φ is noted as the angle between the polarization vector $\boldsymbol{e_i}$ of the incident light and the $\boldsymbol{a}$ axis of the crystals. For the cross-sectional angle-dependent polarized Raman scattering, a polarizer was inserted into the scattering light path to enable the scattered light with polarization parallel to that of the incident laser, namely, $\boldsymbol{e}_i \| \boldsymbol{e}_s$.

Funding. National Natural Science Foundation of China (NSFC) (61427901, 61604178, 91333207, U1505252).

REFERENCES

1. F. Xia, H. Wang, D. Xiao, M. Dubey, and A. Ramasubramaniam, "Two-dimensional material nanophotonics," Nat. Photonics **8**, 899–907 (2014).
2. Y. Gong, J. Lin, X. Wang, G. Shi, S. Lei, Z. Lin, X. Zou, G. Ye, R. Vajtai, B. I. Yakobson, H. Terrones, M. Terrones, B. K. Tay, J. Lou, S. T. Pantelides, Z. Liu, W. Zhou, and P. M. Ajayan, "Vertical and in-plane heterostructures from WS_2/MoS_2 monolayers," Nat. Mater. **13**, 1135–1142 (2014).
3. Q. H. Wang, K. Kalantar-Zadeh, A. Kis, J. N. Coleman, and M. S. Strano, "Electronics and optoelectronics of two-dimensional transition metal dichalcogenides," Nat. Nanotechnol. **7**, 699–712 (2012).
4. W. Zheng, R. Lin, J. Ran, Z. Zhang, X. Ji, and F. Huang, "Vacuum-ultraviolet photovoltaic detector," ACS Nano **12**, 425–431 (2018).
5. A. K. Geim and I. V. Grigorieva, "Van der Waals heterostructures," Nature **499**, 419–425 (2013).
6. W. Zheng, Z. Zhang, R. Lin, K. Xu, J. He, and F. Huang, "High-crystalline 2D layered PbI_2 with ultrasmooth surface: liquid-phase synthesis and application of high-speed photon detection," Adv. Electron. Mater. **2**, 1600291 (2016).
7. M. P. Levendorf, C.-J. Kim, L. Brown, P. Y. Huang, R. W. Havener, D. A. Muller, and J. Park, "Graphene and boron nitride lateral heterostructures for atomically thin circuitry," Nature **488**, 627–632 (2012).
8. X. Zhang, X.-F. Qiao, W. Shi, J.-B. Wu, D.-S. Jiang, and P.-H. Tan, "Phonon and Raman scattering of two-dimensional transition metal dichalcogenides from monolayer, multilayer to bulk material," Chem. Soc. Rev. **44**, 2757–2785 (2015).
9. A. Berkdemir, H. R. Gutiérrez, A. R. Botello-Méndez, N. Perea-López, A. L. Elías, C.-I. Chia, B. Wang, V. H. Crespi, F. López-Urías, J.-C. Charlier, H. Terrones, and M. Terrones, "Identification of individual and few layers of WS_2 using Raman spectroscopy," Sci. Rep. **3**, 1755 (2013).
10. A. C. Ferrari and D. M. Basko, "Raman spectroscopy as a versatile tool for studying the properties of graphene," Nat. Nanotechnol. **8**, 235–246 (2013).
11. H. Li, Q. Zhang, C. C. R. Yap, B. K. Tay, T. H. T. Edwin, A. Olivier, and D. Baillargeat, "From bulk to monolayer MoS_2: evolution of Raman scattering," Adv. Funct. Mater. **22**, 1385–1390 (2012).
12. A. C. Ferrari, J. C. Meyer, V. Scardaci, C. Casiraghi, M. Lazzeri, F. Mauri, S. Piscanec, D. Jiang, K. S. Novoselov, S. Roth, and A. K. Geim, "Raman spectrum of graphene and graphene layers," Phys. Rev. Lett. **97**, 187401 (2006).
13. C. Casiraghi, A. Hartschuh, H. Qian, S. Piscanec, C. Georgi, A. Fasoli, K. S. Novoselov, D. M. Basko, and A. C. Ferrari, "Raman spectroscopy of graphene edges," Nano Lett. **9**, 1433–1441 (2009).
14. K. Gołasa, M. Grzeszczyk, P. Leszczyński, C. Faugeras, A. A. L. Nicolet, A. Wysmołek, M. Potemski, and A. Babiński, "Multiphonon resonant Raman scattering in MoS_2," Appl. Phys. Lett. **104**, 092106 (2014).
15. A. A. Mitioglu, P. Plochocka, G. Deligeorgis, S. Anghel, L. Kulyuk, and D. K. Maude, "Second-order resonant Raman scattering in single-layer tungsten disulfide WS_2," Phys. Rev. B **89**, 245442 (2014).
16. G. L. Frey, R. Tenne, M. J. Matthews, M. S. Dresselhaus, and G. Dresselhaus, "Raman and resonance Raman investigation of MoS_2 nanoparticles," Phys. Rev. B **60**, 2883–2892 (1999).
17. K. F. Mak, C. Lee, J. Hone, J. Shan, and T. F. Heinz, "Atomically thin MoS_2: a new direct-gap semiconductor," Phys. Rev. Lett. **105**, 136805 (2010).
18. W. Zhao, Z. Ghorannevis, L. Chu, M. Toh, C. Kloc, P.-H. Tan, and G. Eda, "Evolution of electronic structure in atomically thin sheets of WS_2 and WSe_2," ACS Nano **7**, 791–797 (2013).
19. A. C. Ferrari, "Raman spectroscopy of graphene and graphite: disorder, electron-phonon coupling, doping and nonadiabatic effects," Solid State Commun. **143**, 47–57 (2007).
20. L. G. Cancado, A. Jorio, E. H. Martins Ferreira, F. Stavale, C. A. Achete, R. B. Capaz, M. V. O. Moutinho, A. Lombardo, T. S. Kulmala, and A. C. Ferrari, "Quantifying defects in graphene via Raman spectroscopy at different excitation energies," Nano Lett. **11**, 3190–3196 (2011).
21. J. P. Perdew, K. Burke, and M. Ernzerhof, "Generalized gradient approximation made simple," Phys. Rev. Lett. **77**, 3865–3868 (1996).
22. W. Zheng, F. Li, G. Li, Y. Liang, X. Ji, F. Yang, Z. Zhang, and F. Huang, "Laser tuning in van der Waals crystals," ACS Nano **12**, 2001–2007 (2018).
23. J. Kang, S. Tongay, J. Zhou, J. Li, and J. Wu, "Band offsets and heterostructures of two-dimensional semiconductors," Appl. Phys. Lett. **102**, 012111 (2013).
24. M. Cardona and G. Guntherodt, *Light Scattering in Solids II* (Springer, 1982).
25. W. Zheng, R. Zheng, F. Huang, H. Wu, and F. Li, "Raman tensor of AlN bulk single crystal," Photon. Res. **3**, 38–43 (2015).
26. C. Kranert, C. Sturm, R. Schmidt-Grund, and M. Grundmann, "Raman tensor formalism for optically anisotropic crystals," Phys. Rev. Lett. **116**, 127401 (2016).
27. C. Kranert, C. Sturm, R. Schmidt-Grund, and M. Grundmann, "Raman tensor elements of β-Ga_2O_3," Sci. Rep. **6**, 35964 (2016).
28. W. Zheng, J. Yan, F. Li, and F. Huang, "Elucidation of 'phase difference' in Raman tensor formalism," Photon. Res. **6**, 709–712 (2018).
29. H. J. Monkhorst and J. D. Pack, "Special points for Brillouin-zone integrations," Phys. Rev. B **13**, 5188–5192 (1976).
30. S. M. Heald and E. A. Stern, "Anisotropic X-ray absorption in layered compounds," Phys. Rev. B **16**, 5549–5559 (1977).